THE ASTROPHYSICAL JOURNAL, 341:456–473, 1989 June 1

DOPPLER IMAGING OF ABUNDANCE FEATURES ON Ap STARS: THE Si II DISTRIBUTION ON γ^2 ARIETIS[1]

ARTIE P. HATZES, G. DONALD PENROD, AND STEVEN S. VOGT
Lick Observatory, Board of Studies in Astronomy and Astrophysics, University of California, Santa Cruz
Received 1988 April 11; accepted 1988 October 28

ABSTRACT

We present an application of the Doppler imaging technique to the mapping of the surface distribution of elements on rapidly rotating magnetic Ap stars. This method uses the principles of maximum entropy image reconstruction to iteratively solve a matrix equation relating the local equivalent width distribution on the surface of a star to the observed spectral line profile variations. It is shown, using synthetic spectral data, that this method can accurately recover complex features in test images. The method also can recover regions of enhanced as well as depleted abundances in spite of the assumption that the line shapes are the same for both regions. We also present a modified version of technique which accounts for the nonlinear change in local line shapes with equivalent width. Using high signal-to-noise ratio and high-resolution spectral line profiles obtained at Lick Observatory, this technique was used to derive the equivalent width map of the Si II λ6437 Å line in γ^2 Ari. This map consists of two circular spots of depleted abundance, one of which is surrounded by an incomplete annulus of enhanced abundance. The spots coincide with the previously known longitudinal position of the magnetic poles. The derived silicon image suggests that silicon is depleted where field lines are vertical and is enhanced near where the field lines are horizontal, thus providing strong direct observational evidence that the selective diffusion of elements in the presence of a magnetic field is responsible for the abundance variations in these stars.

Subject headings: stars: abundances — stars: individual (γ^2 Ari) — stars: magnetic — stars: peculiar A

I. INTRODUCTION

The magnetic Ap stars represent the largest subclass of a group of stars known collectively as the chemically peculiar stars and are characterized by the presence of large (~kilogauss), time-variable magnetic fields. Stibbs (1950) first proposed that the magnetic variations are due to the presence of a large dipole field whose axis is inclined to the rotation axis of the star (oblique rotator model). These stars also exhibit photometric and spectral variations which are believed to be due to the inhomogeneous distribution of chemical elements across the stellar surface. Clearly the surface distribution of elements is intimately related to the presence of the magnetic fields and the ability to derive this distribution is central to understanding the nature and role of the magnetic field in the atmospheres of these stars.

The problem of deriving the abundance distribution on the surface of a star from the spectral variations has been attempted by several investigators. The first technique was developed by Deutsch (1970), who assumed that the distribution of local equivalent widths on the surface of the star could be expanded as a series of spherical harmonics. A similar expansion could be made for the observed radial velocity and magnetic field variations thus establishing a system of equations which could be solved for the expansion coefficients. However, a major drawback of this technique was that in order to solve the equations, the expansion series had to be truncated after only a few terms, thus restricting the complexity of the features that could be discerned. Also the technique used the integral characteristics of the line profiles, thus ignoring the line shapes, where most of the information is contained.

Several researchers attempted to improve on the Deutsch method by including information about the line shapes. Pyper (1969) and Mégessier (1975) chose to divide the spectral line into components and assign a particular "spot" on the stellar surface responsible for each component. As pointed out by Pavlova, Khokhlova, and Aslanov (1977) this was subject to arbitrariness and produced unpredictable errors. Another major fault of this modification is that one *a priori* chooses the type of spots found on the surface, that is, whether they have enhanced or depleted abundance. For instance, if a single spot of depleted abundance is present on the surface then the resulting line profile shape, when the spot is crossing the line of sight, is one with a small emission bump in the core. This gives the line profile a double-line appearance, and using component analysis one would conclude that this splitting was due to two distinct patches of overabundance on the surface. In this case breaking the line into separate components utterly fails at recovering the number and type (depleted vs. enhanced) of abundance spots. This stresses the importance of using a mapping technique which is unrestrained in the type and number of spots it is permitted to find. The resulting distribution should be dictated by the data, not a researcher's prerogative. Further modifications to the Deutsch technique were suggested by Falk and Wehlau (1974) and Mihalas (1973).

The method of Goncharsky *et al.* (1982) resulted in the first solution of the inverse problem of mapping the local equivalent width on the stellar surface from the *shapes* of the observed spectral line profiles (and not just integrated quantities). Their technique involved solving an integral equation which related the observed spectral line profiles to the local equivalent width integrated over the stellar surface. This method was applied to α^2 CVn, CU Vir, and χ Ser by Goncharsky *et al.* (1983), ϵ UMa by Rice *et al.* (1981), and more recently to θ Aur by Khokhlova, Rice, and Wehlau (1986). The resulting abundance maps had various degrees of complexity. The Eu distribution for α^2 CVn consisted of two enhanced abundance spots near the magnetic

[1] *Lick Observatory Bulletin*, No. 1122.

poles. Two spots of enhanced abundance (not always 180° apart) also characterized the silicon distribution for CU Vir, the chromium distribution for ϵ UMa, and the strontium distribution for χ Ser. The distribution of elements for θ Aur was the most complex, exhibiting a single spot for the strong λ4924 Å Fe II line but up to six spots of enhancements for weaker iron lines as well as chromium and silicon lines. The resulting maps did not always have an obvious relationship to the magnetic field configuration and the location of many features tended to favor the sub-observer latitude.

In a previous paper (Vogt, Penrod, and Hatzes 1987, hereafter Paper I) we outlined a version of the Doppler imaging technique which incorporated the maximum entropy formalism. The motivation for developing this technique was to study the brightness distribution on the spotted RS CVn and FK Comae stars. In the course of these studies we realized that the technique could also be applied to the Ap stars with only slight modifications. In the present paper we describe the technique as applied to Ap stars and discuss the differences between mapping abundance distributions as opposed to brightness distributions. The success as well as the failings of the mathematical technique at recovering known abundance distributions on a star is evaluated. Finally in § VI the method is used to derive the local equivalent width map of the Si II λ6347 Å line in the ApSiCr star γ^2 Ari.

II. INVERTING THE LINE PROFILES

a) *Doppler Imaging*

The success of any inversion technique can be vastly improved by using the line shapes, thus utilizing the Doppler information to its fullest extent. In Paper I we outlined the Doppler imaging technique and the requirements needed for the imaging candidate. This technique takes advantage of the fact that for a stellar line profile whose line shape is dominated by rotational Doppler broadening, there is a one-to-one mapping between wavelength position in the line and corresponding spatial position on the star. Any inhomogeneities in the stellar atmosphere (temperature, composition, etc.) across the surface of the star will be reflected as distortions in the line profile shapes, which change as the star rotates. In the Ap stars these spectral distortions are caused by variations in the chemical abundance across the stellar surface.

If a "spot" on the surface of a star has an abundance which is enhanced with respect to the mean "photospheric" value, then the stronger absorption in the spot will cause a dip (with respect to an immaculate, rotationally broadened profile) to appear in the absorption line profile. Likewise a spot with depleted abundance will have a weaker line strength and will contribute less absorption to the integrated line profile, thus resulting in an emission bump appearing in the line. The height (depth) of the bump (dip) depends on the line strength difference between spot and photosphere, the ratio of continuum brightness, and on the fraction of the constant radial velocity chord across the star which is contained in the spot. Regions of the stellar surface lying on constant radial velocity chords are mapped into the same region of the spectral line causing a latitudinal ambiguity of spot position. However, if a star has an intermediate inclination ($30° < i < 70°$), then much of this ambiguity is removed by observing the star at several rotation phases. The line profile shape at a given phase thus represents a one-dimensional projection of the surface distribution of an element, but by observing the star at different rotation phases one is able to obtain projections at different aspect angles. The inverse problem is now reduced to using a sequence of time-resolved one-dimensional spectra to reconstruct a two-dimensional map of the surface distribution of elements.

b) *Matrix Formulation of the Inverse Problem*

The inverse problem can be stated conveniently by a matrix equation as described in detail in Paper I. The stellar surface is first divided into n equal area cells with the same zone geometry used in Paper I. These cells are unwrapped to form an image vector $\boldsymbol{I}$ of n elements. The value I_j is just the local equivalent width, W_λ, of a spectral line produced by the stellar surface at pixel j. If a spectral line of the star consisting of m_s points is observed at m_p phases of the stellar rotation, a data vector $\boldsymbol{D}$ of m elements can be constructed such that $m = m_s \times m_p$. A transfer matrix $\boldsymbol{R}$ then provides the mapping from image space into data space. In matrix notation this is written as

$$\boldsymbol{I} \cdot \boldsymbol{R} = \boldsymbol{D} . \tag{1}$$

This matrix equation essentially represents a system of m equations which have to be solved for the n variables $(I_1, I_2, \ldots, I_n)$.

Each matrix element, R_{jk}, represents the marginal response of data pixel D_k to changes in image pixel I_j or equivalently $R_{jk} = \partial D_k / \partial I_j$. The transfer matrix, $\boldsymbol{R}$, contains all the assumptions about the atmospheric physics and physical parameters of the star. In constructing the matrix elements an approximation is needed for the local line shape produced by a stellar image pixel I_j. Rather than using a Gaussian profile or some other approximation, we chose to generate specific intensity profiles using ATLAS5 subroutines and model atmospheres from Kurucz (1979). Unfortunately, these atmospheric models are for normal A stars and do not include effects due to the presence of large magnetic fields or the peculiar composition of the stellar atmospheres of Ap stars. Although we may eventually try to use full radiative transfer in a magnetic field, we find that the present simpler approach does not provide a severe restriction to the technique when properly applied. All the stars in our study are rapid rotating and the line profile shapes are dominated by rotational broadening, even for the largest measured magnetic fields in these stars. The inclusion of magnetic fields will cause the specific intensity profiles to have a slightly different shape than those formed in the absence of magnetic fields, and we will demonstrate in § IV that the method is insensitive to wrong assumptions about the intrinsic line shapes. Another effect of the magnetic fields is an increase in the equivalent width of the line due to desaturation of strong lines caused by Zeeman splitting. This also should present no problems as the reconstructed image is simply of the local equivalent width (not abundance) of a spectral line on the surface of the star. The more difficult problem of converting this equivalent width to a real *abundance* does require a detailed knowledge of the atmospheric physics, including magnetic effects. We therefore believe that the specific intensity profiles produced by these standard models are an adequate approximation for the local line shapes found in the Ap stars of this study.

In constructing the matrix elements, the partial derivative $\partial D_k / \partial I_j$ is approximated by the ratio I_λ / W_λ, where I_λ is the specific intensity profile and W_λ is the equivalent width of the total profile. (Henceforth the specific intensity profiles which are divided by the equivalent width of the profiles shall be referred to as the marginal specific intensity profiles.) Inherent in this approximation is the assmption that the line shape is

independent of the equivalent width of the line, which is not strictly true; strong lines have broader wings and larger full width at half maximum than weaker lines. This was not a problem in mapping the brightness distributions on spotted late-type stars since the spots are so cool that they contribute little to the integrated line flux. Thus the different shape of the instrinsic line profile found in the spot is not as important. Abundance spots in Ap stars contribute significantly to the integrated flux and complications may arise if there are large variations in W_λ across the star and the assumption of constant line shapes breaks down. In § IV*e* we examine the effects of this assumption on the resulting image solution, and in § V we present a modified version of our technique which can account for the nonlinear change in line shapes with increasing line strength.

The transfer matrix is arranged so that row j contains the marginal specific intensity profiles for pixel j. The first m_s elements are the marginal profiles for the first observed phase, the second set of m_s elements for the second phase, etc. The matrix is constructed as follows. The location on the stellar surface (in a fixed coordinate system) for pixel j at the first observed rotational phase is calculated. This location determines the following phase-dependent quantities: (1) the appropriate specific intensity profile for that particular limb angle, (2) the projected area of the pixel (if it is not visible at that phase the area is set to zero), and (3) the radial velocity of the pixel (this requires a knowledge of the rotational velocity as well as the inclination of the star.) The marginal specific intensity profiles appropriate for the current limb angle of the stellar pixel are then Doppler-shifted by the pixel's radial velocity, scaled by the pixel's projected area, and inserted into the first m_s columns of the first row. This is repeated for the remaining pixels on the stellar surface for the first phase thus determining the first m_s columns for all rows. The star is then rotated to the next observed phase and the above quantities are calculated for all stellar pixels at that phase. This determines the next m_s columns of the matrix. The procedure continues until the entire matrix is computed. Paper I gives examples of the appearance of this transfer matrix.

III. MAXIMUM ENTROPY IMAGE RECONSTRUCTION

Mathematically the inverse problem for mapping abundance distributions from spectral lines is now reduced to solving equation (1). Formally a solution for the image vector can be found by inverting the transfer matrix $\boldsymbol{R}$ such that $\boldsymbol{I} = \boldsymbol{R}^{-1}\boldsymbol{D}$. In practice this is difficult. The fact that the local line profiles of pixels lying along a constant radial velocity chord are projected into the same wavelength location in the observed spectral lines suggests that some of the rows of $\boldsymbol{R}$ are dependent (invertibility of a matrix requires that it be square and with independent rows). Thus any solution we find is necessarily nonunique. Even if the matrix were invertible (least-squares techniques could be used on nonsquare matrices), there are several reasons for avoiding the direct inversion approach. First, direct inversion is more susceptible to the presence of noise in the data. Second, the straight unconstrained inversion has no knowledge of adjacency of pixels, and this can lead to the unphysical situation where adjacent pixels can have unphysically large variations in their values and yet still satisfy the observed data.

In Paper I we outlined an iterative scheme for inverting the matrix equation using maximum entropy digital image reconstruction. The entropy of an image is defined as

$$S = -\sum_j p_j \log (p_j) , \tag{2}$$

where $p = I_j/\sum I_j$, the normalized positive pixel values of the image (in this case I_j is the value of the local equivalent width at pixel j). S represents the *negative* of the information content of an image. Thus the image with the maximum entropy is the one with the least amount of spatial information and is thus the "smoothest" or "simplest" image. Using the entropy has several advantages. First, if the solution is nonunique, maximum entropy will find the simplest solution to the observed data, and since the maximum entropy solution has the minimum amount of information, any structure or features present in the image is required by the data. More complex solutions may exist, but they cannot be uniquely determined from the data set. Second, equation (2) ensures that throughout the reconstruction process pixel values remain nonnegative ($W_\lambda > 0$). Finally, the maximum entropy solution represents the smoothest image and this avoids dramatic, physically unreal variations of nearby pixel values, something that would have to be incorporated into any direct inversion technique. For a solution to be valid it must satisfy the constraint that it fit the observed data set to some required level of accuracy, usually set by the noise level. If d_k represents the observed data values and g_k represents the theortical data values which result from our solution image, then a convenient measure of the misfit between the two is

$$\chi^2 = \sum_k (g_k - d_k)^2/\sigma_k^2 . \tag{3}$$

The uncertainty of each data element is given by σ_k. The technique of maximizing S subject to the constraint $\chi^2 = \chi_0^2$, where χ_0^2 is the desired fit is commonly referred to as the maximum entropy method (Skilling and Bryan 1984). The required maximum will be the extremum of the function

$$Q = S - \lambda\chi^2 , \tag{4}$$

where λ is a Lagrange multiplier. The maximum entropy software, MEMSYS, developed by Gull and Skilling (Skilling and Gull 1981) is used to find this extremum. This algorithm uses the transfer matrix $\boldsymbol{R}$ and, as an approximation for the inverse, the transpose $\boldsymbol{R}'$, to transform between image and data space. The extremum of the function S is found using conjugate gradient search techniques. We found the algorithm to be fast and efficient. A final image solution is accomplished in 15–20 iterations using 30–40 minutes of CPU time on a VAX 11/780 computer. This iteration scheme requires a starting guess for the image solution, which is usally taken to be a uniform array of equivalent width values typically taken to be the mean equivalent width of the observed line profiles. As demonstrated in Paper I the method finds the same solution regardless of the initial guess. The only constraints on the final solution is that the pixel values are positive, and that the final image fit the observed data to within the uncertainty of each data pixel (specified by eq. [3]). The technique is thus free to choose between enhanced or depleted abundance spots and the final choice is dictated by the distribution that provides the best fit to the observed data.

IV. TESTS OF THE METHOD

The ability of the method to recover the local equivalent width map strictly from the line profile variations was evaluated for several test images of artificial stars with abundance

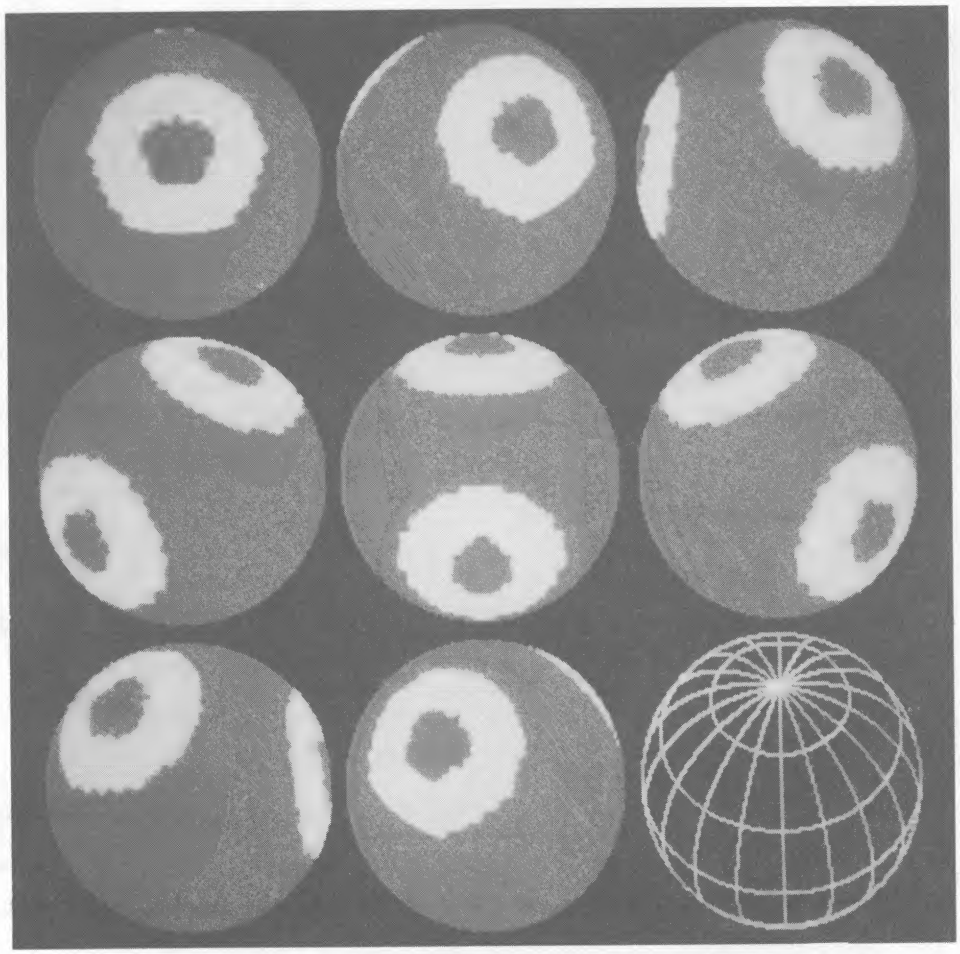

FIG. 1.—Test input image consisting of two overabundant (W_λ = 280 Å) rings (photosphere W_λ = 130 mÅ). Shown here are eight views of the star at intervals of 0.125 in phase. Phase 0.0 is the upper left-hand globe, and the sequence proceeds from left to right and top to bottom. The phantom star at the lower right illustrates the location of the rotation pole.

distributions of varying degrees of complexity. Since the technique is similar to that used in Paper I in deriving the brightness on the spotted RS CVn stars, many of the tests carried out in that article such as signal-to-noise ratio effects and tests of incomplete phase coverage will not be repeated here. The reader should refer to that paper for a discussion of these tests. The spectral type of our artificial star was taken to be A0 V, and the Si II λ6347 line was used in generating the data sets. In each case, line profiles at 16 equally spaced phases were generated using an explicit disk integration scheme with a zone geometry different from that used in the reconstruction procedure. These synthetic data were then used by the MEMSYS software to obtain an equivalent width map across the surface of the star. In generating the synthetic data, true specific intensity profiles appropriate to the local equivalent of the spot region were used as opposed to scaled versions of the same line profile used by the reconstruction procedure. The line profile in each "spot" thus has the true line shape appropriate for the local equivalent width. In the discussion that follows the term "spot" shall refer to any distribution on the surface of the star having an equivalent width different from the mean or photospheric value. The term *overabundance* is used to describe any distribution which has a local equivalent width greater than the mean value across the stellar surface and is not to be interpreted as being a true overabundance with respect to normal, non-peculiar stars with the same spectral type. Likewise the term *underabundance* is used to describe any region having a local equivalent width less than the mean value over the stellar surface.

a) The "Two-Ring Test"

The first test case consists of two overabundant rings (inner radius = 15°, outer radius = 35°), one centered at latitude 60° and the second at latitude of 10°. The input image is shown in Figure 1. This image as in all subsequent images of this type shows the star at eight equally spaced phases (increments of 0.125) starting with phase 0.0 in the upper left-hand corner. The phantom star at the lower right shows the orientation of the rotation axis of the star. The local equivalent width in the rings is 280 mÅ while the photospheric value is 130 mÅ. A $v \sin i$ of 60 km s^{-1} and an inclination of 40° were used in this example. A transfer matrix was constructed using the appropriate stellar parameters and specific line intensity profiles having equivalent widths of 200 mÅ. This value was chosen as it represented the mean value of the measured equivalent width for the observed line profiles. The shape of this specific intensity profile is slightly different than that found in either the photosphere or the spots.

Figure 2 shows the synthetic line flux profiles (*crosses*) at 16 equidistant phases which were then used by MEMSYS to

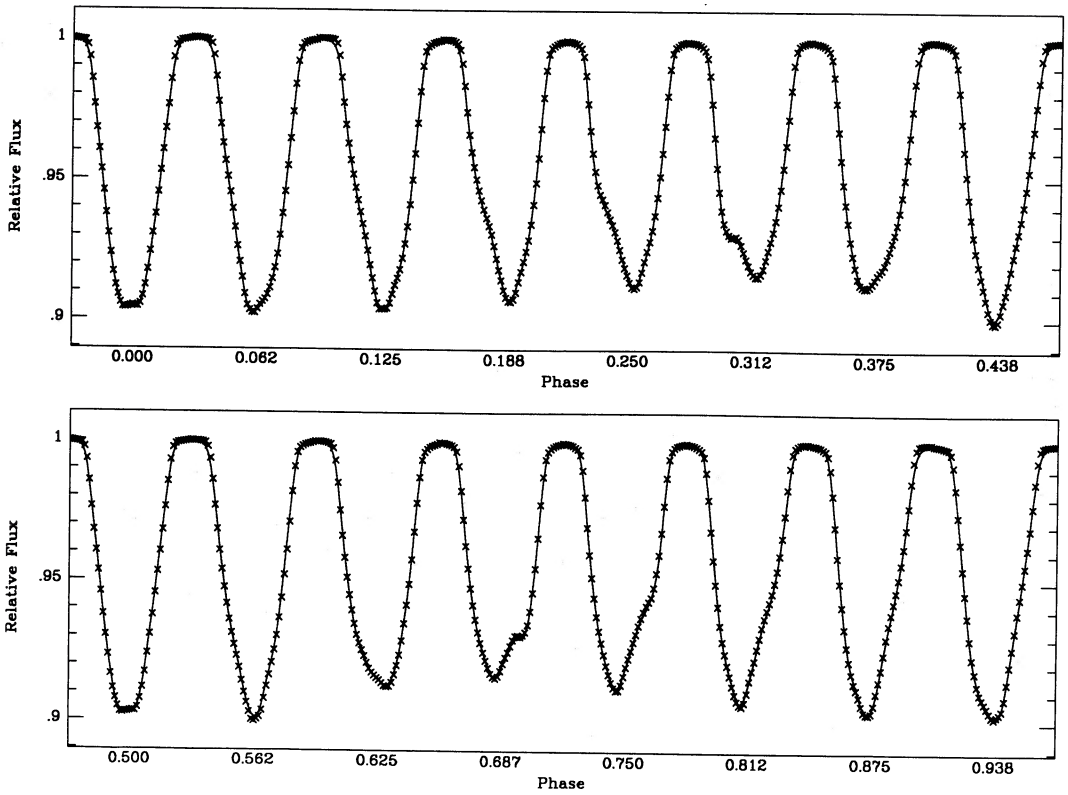

FIG. 2.—Synthetic spectral line flux profiles from the "two-ring" test image of Fig. 1. These flux profiles are for the Si II 6347 line at 16 equidistant phases. The theortical profiles are shown as crosses and the reconstruction software's final fit (after 15 iterations) is shown by the solid line. The ordinate is the relative intensity normalized to unity in the continuum.

reconstruct the local equivalent width. The ordinate of this figure represents the relative flux normalized to unity in the continuum. Figure 3 shows the maximum entropy reconstruction of the two-ring case. The line fits resulting from this map are drawn as lines in Figure 2. For the equivalent width map, regions with higher equivalent width than the mean value over the star are shown as white with respect to a gray photosphere. A comment is in order here concerning this reconstructed image and the subsequent ones which are displayed. In all images, regions of depleted abundance appear as black and regions of enhanced abundance (with respect to the mean value over the stellar surface) appear as white. In the actual reconstructed images there is a smooth variation in the equivalent width from regions of the photosphere to regions of enhanced or depleted abundance. We found (through our experience with Paper I) that the gray scale of the published images did a poor job of reproducing with clarity the subtle variations of the equivalent width in a region (this was especially true when trying to show both enhanced and depleted abundance regions). This lack of clarity would only be a source of confusion. As a result we were compelled to publish a high-contrast version of our images. For regions of enhanced abundances, all image pixel values above a certain level were set to the same shade of white and for depleted regions all values of the equivalent width below a threshold value were set to the same shade of black. Although it improves the clarity in the published figures, this procedure does have the disadvantage in that regions with different values in the equivalent width are shown with the same intensity. In the text we shall point out if largely differing values of the equivalent width are displayed with the same gray level.

For the ring lying at higher latitudes, the technique does an excellent job of recovering the true shape and location of the ring. As expected the technique does a poorer job at recovering the lower latitude ring due to geometrical foreshortening. The low-latitude pixels which constitute the lower ring have a smaller projected area. Thus their contribution to the integrated line profiles is smaller than for the high-latitude pixels found in the upper ring. As a result MEMSYS has less information on the lower ring and thus does a poorer job at reconstructing it. The method does, however, recover the upper arc of the ring and is able to discern that the lower latitude feature is more complex than can be accounted for by a simple, circular spot.

One artifact of the maximum entropy technique is that it tends to smooth or blur features and this blurring is more severe for low latitude features due to their small projected area. (Unfortunately, the high-contrast maps fail to show this.) A direct result of this blurring is that it decreases the equivalent width of the spot in the reconstructed image from its true input value. This smoothing in effect causes a slight increase in the area and as a result the spot need not have as large an equivalent width to fit the line profile. For the spotted RS CVn stars, photometry can be used to independently determine the spot temperature. For the Ap stars the local equivalent width in a spot can be determined only from the spectral line profiles and hence the reconstructed map. Therefore, it is of interest to evaluate the accuracy of the technique at recovering the *true* equivalent width of a spot.

This was done by creating a test image of several overabundant spots ($W_\lambda = 280$ mÅ) at various latitudes and examining the local equivalent width of the spot in the recon-

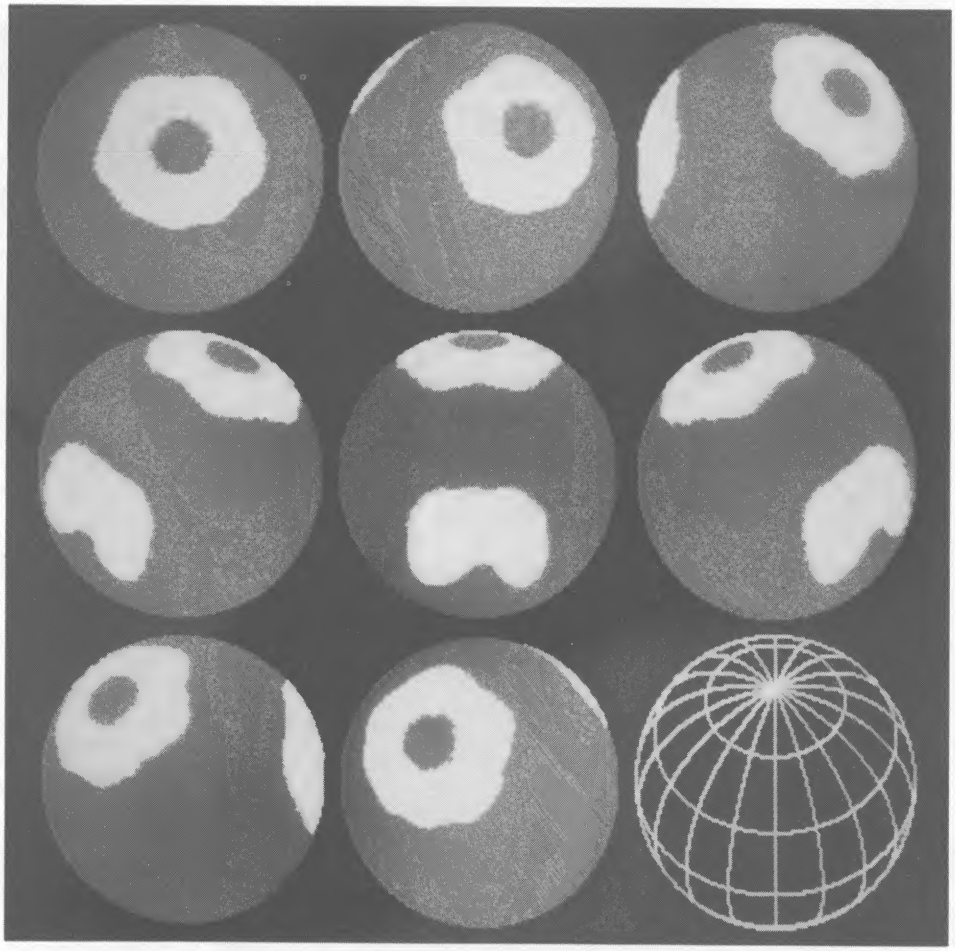

FIG. 3.—Doppler image recovery of the "two-ring" image of Fig. 1, from the synthetic line flux data of Fig. 2

structed map as a function of latitude. An inclination of 50° and a $v \sin i$ of 50 km s^{-1} were used in this simulation. We found that local equivalent width of the reconstructed spots was lowered from 280 mÅ to 210 mÅ. This recovered equivalent width was reasonably constant down to a latitude of 30° (20° below the subobserver latitude) below which it dropped sharply to about 165 mÅ at the equator. This is due to the geometrical foreshortening of these low latitude pixels as stated earlier. For regions of enhanced abundance we can thus expect the recovered equivalent width to be slightly lower than the true value.

b) *Depleted and Enhanced Spot Distributions: The Ring-Spot-X Test Case*

The method is unconstrained in its choice of whether a region has depleted or enhanced abundances. Therefore the ability of the technique to recover both types of spots should be examined. This is important in light of the fact that the same line shapes are assumed for both spot regions as well as the photosphere and this assumption may compromise the method's ability in reconstructing distributions having local line shapes drastically different from the assumed shape.

For this test an input image consisting of an overabundant annulus ($W_\lambda = 400$ mÅ) surrounding an underabundant spot ($W_\lambda = 25$ mÅ) centered at latitude 10° was created. A group of underabundant spots $W_\lambda = 25$ mÅ in the shape of an "X" was also placed at latitude 55°. Once again the photospheric local equivalent width was 130 mÅ. For this case the star had an inclination of 40° and a projected rotational velocity of 60 km s^{-1}. Once again matrix elements were constructed using specific intensity profiles whose shapes were consistent with those having an equivalent width of 200 mÅ. This input image is shown in Figure 4. In this figure, regions of enhanced abundances with respect to the mean (gray) photosphere are shown as white, while those of depleted abundances are shown as black.

The resulting maximum entropy reconstruction is shown in Figure 5 and the fits to the line profiles in Figure 6. The technique once again does an excellent job at recovering all features in spite of the fact that the line shape in the overabundant ring is significantly different from that of the underabundant spots. Once again the technique had some difficulty reconstructing the low-latitude regions of the ring.

c) $v \sin i$ *and Limb-darkening Effects*

As pointed out in Paper I, incorrect assumptions about the $v \sin i$ of the star leads to noticeable effects in the final reconstructed image. In the case of equivalent width mapping, choosing too large a $v \sin i$ in constructing the transfer matrix should lead to an underabundant band circling the star near the equator. The reason for this is simple. The true line shapes are narrower than those produced by the transfer matrix. The

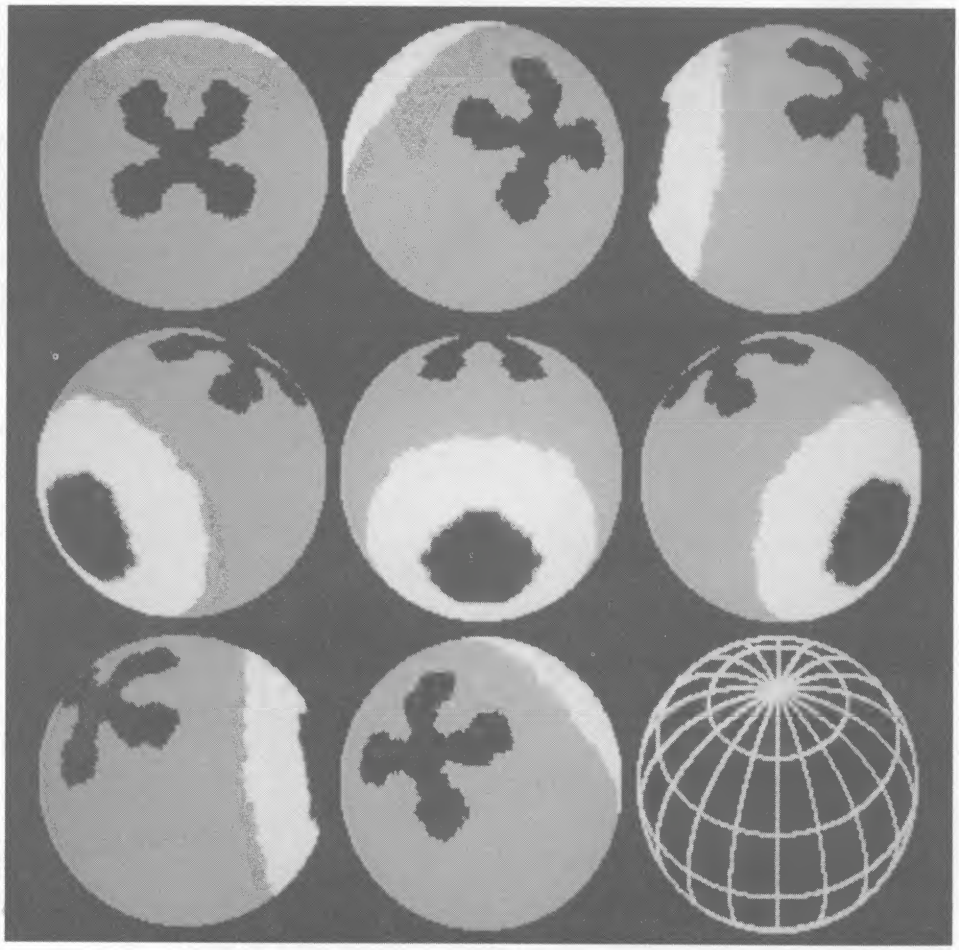

FIG. 4.—Test input image consisting of an enhanced abundance ring ($W_\lambda = 400$ mÅ, shown as white) surrounding a depleted spot ($W_\lambda = 25$ mÅ, shown as black) and a depleted "X" ($W_\lambda = 25$ mÅ).

only way for MEMSYS to produce narrower lines is to place underabundant features on regions of the star that are always in view, namely bands circling the star or features at the rotation pole. As a test, a set of immaculate profiles (from a uniform star) were generated which had a true $v \sin i$ of 50 km s^{-1} and an equivalent width of 150 mÅ. A matrix was constructed using an assumed $v \sin i$ of 52 km s^{-1} and a solution to the synthetic profiles found. The maximum entropy reconstruction attempted to "narrow" the line shapes by putting a slightly depleted band (minimum $W_\lambda = 140$ mÅ) near the equator. To preserve the equivalent width of the observed (integrated) profiles, the method also placed a slightly overabundant cap at the pole (maximum $W_\lambda = 190$ mÅ). Likewise an underestimate of the $v \sin i$ by 2 km s^{-1} caused an overabundant band (maximum $W_\lambda = 170$ mÅ) to appear at the equator and a depleted cap (minimum $W_\lambda = 140$ mÅ) to appear at the pole.

An incorrect limb-darkening law for the specific intensity profiles also causes spurious features to appear with a symmetry about the rotation axis of the star. Increasing the limb darkening tends to make the stellar profiles more "V"-shaped, that is, it makes the cores deeper and the wings narrower. We thus expect a limb-darkened line profile to mimic a non–limb-darkened profile but with smaller $v \sin i$. As a test, line profiles were generated using a continuum limb-darkening constant of $\epsilon = 0.5$, a $v \sin i$ of 50 km s^{-1}, and an equivalent width of 150 mÅ. Two transfer matrices were constructed using limb-darkening laws of $\epsilon = 0.05$ and 0.8. The matrix constructed with too little limb darkening produced an image with an underabundant band (minimum $W_\lambda = 130$ mÅ) near the equator and an overabundant cap (maximum $W_\lambda = 190$ mÅ) at the pole, similar in appearance to the reconstruction using too large a $v \sin i$. The matrix with elements having more limb darkening than the stellar profiles produced an overabundant band (maximum $W_\lambda = 190$ mÅ) near the equator, and a depleted cap (minimum $W_\lambda = 100$ mÅ) at the pole, similar to the image using too small a rotational velocity for the matrix elements.

Spurious features arising from wrong assumptions about the projected rotational velocity or the limb darkening of a star are thus characterized by their symmetry about the rotational axis (a band at the equator and spot at the pole). Even grossly wrong assumptions about these quantities produce low-level features which do not corrupt the shapes and locations of true features on the stellar surface. It is advantageous that limb-darkening effects mimic $v \sin i$ effects in that uncertainties in the limb darkening law can be canceled by the appropriate choice of projected rotational velocity, an easy parameter to change.

d) Inclination Effects

None of our sample of stars are binaries with known orbits; thus it is impossible to obtain an independent determination

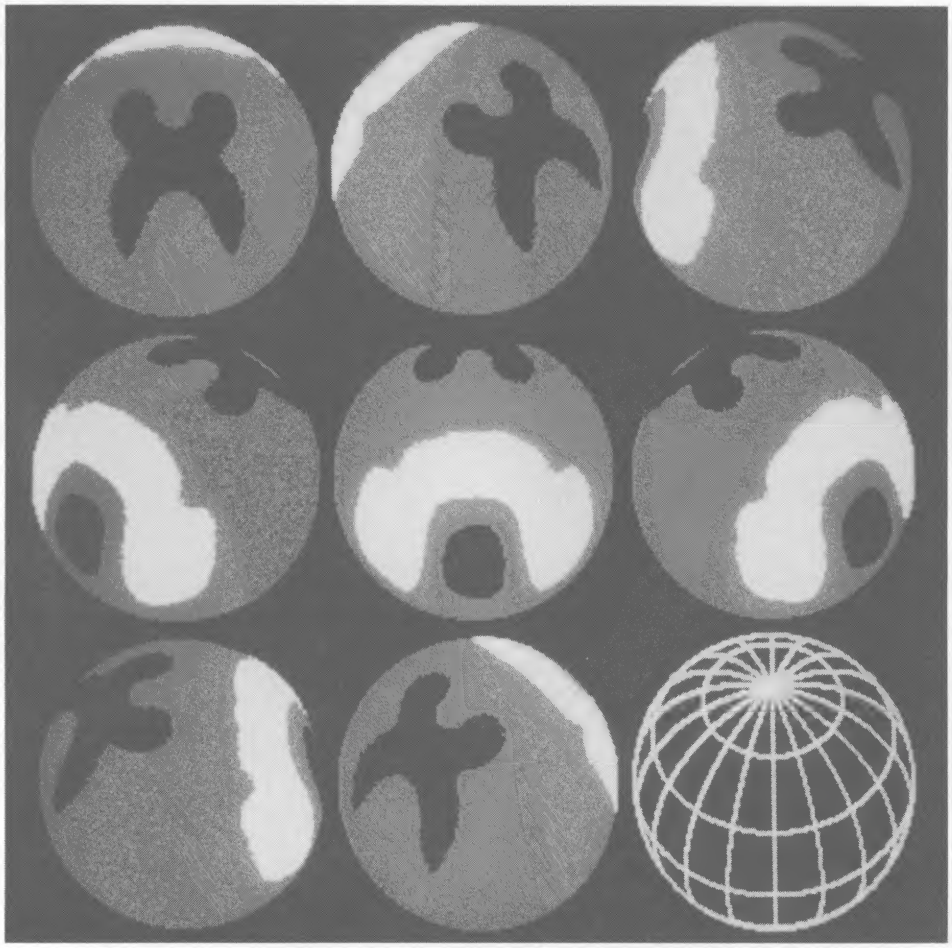

FIG. 5.—Doppler image recovery of the "ring-spot-X" test image of Fig. 4

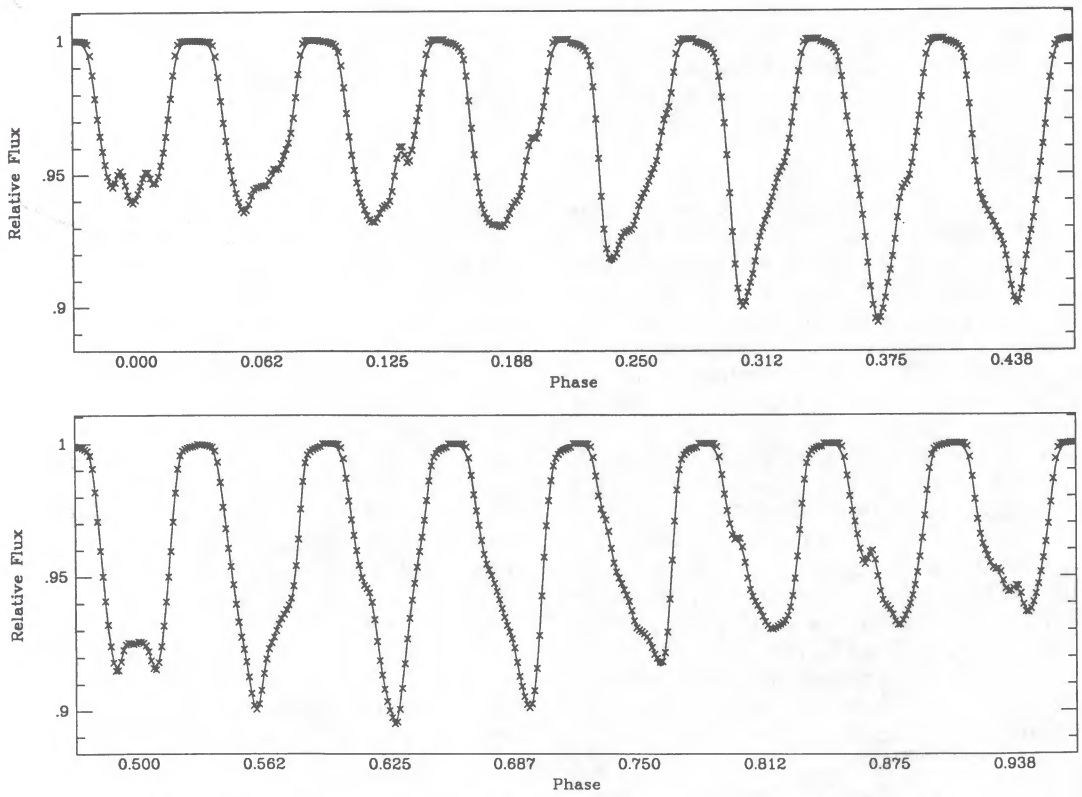

FIG. 6.—Synthetic spectral line flux profiles for the "ring-spot-X" test image of Figs. 4 and 5

of the inclination of the star. In Paper I we showed that the maximum entropy method was largely insensitive to wrong assumptions about the inclination of the star. For spots lying at high latitudes, changing the inclination of the star used in construction of the transfer matrix to a value different than that used in generating the data set did not alter the shape or location of the spot distribution. This is due to the fact that the latitude of a spot is determined by the speed at which it crosses the line profile and this is a function only of stellar latitude. However, this independence on assumed inclination can only go so far. For a transfer matrix constructed using the wrong inclination, there is an inconsistency at the lowest and highest latitudes between visible pixels in the matrix and those which are actually visible on the star. We thus should expect some changes in the image solution for these pixels when the assumed inclination is grossly wrong. Although the final image is insensitive to moderate changes in the inclination, the technique may actually be able to indicate whether one is using an unreasonably wrong value for the inclination.

To investigate this effect in greater detail, a data set was constructed using the two-ring spot distribution in § IV*a* and with an inclination of 50° for the star. Solutions were obtained using different transfer matrices generated with stellar inclinations ranging from 25° to 75°. All solutions were able to reconstruct the high-latitude ring. For the case $i = 25°$, however, there are fewer low-latitude pixels available for the matrix to change than are actually visible on the star. The technique compensated by greatly increasing the equivalent width of the spot pixels in the lower ring (maximum $W_\lambda = 300$ mÅ). A similar effect occurred in the case $i = 75°$. For this inclination many of the high latitude pixels are thought to be invisible at certain phases by the transfer matrix when actually they *are* in view. Once again the technique compensated by increasing the equivalent width of these spot pixels to a maximum of about $W_\lambda = 300$ mÅ. As a comparison, the maximum pixel values for a reconstruction made with the proper inclination is about 230 mÅ.

This effect can be seen more clearly in Figures 7*a* and 7*b*, where we have plotted the constrast and the entropy (as defined by eq. [2]) as function of inclination used in the transfer matrix. The contrast is defined as

$$C = (I_{\max} - I_{\min})/I_{\text{avg}} , \quad (5)$$

where $I_{\max}$, $I_{\min}$, and I_{avg} are the maximum, minimum, and average pixel values of the final image, respectively. The contrast is minimized near an inclination of 60°, while the entropy is maximized for this value (as expected since the image with the lowest contrast should be a maximum entropy image). This value is near but not at the true value of 50° used in generating the spectral data set. We should also mention that the rate of convergence for the various solutions were also minimized near this value of 60°.

Using the contrast, entropy, and rate of convergence are second-order, subjective effects. A more objective effect would be how well each image fits the observed profiles and indeed the best fit to the data is obtained when the correct inclination is used in the transfer matrix. In Figure 7*c* the value of χ^2 as defined in equation (3) is plotted as a function of the inclination used in the transfer matrix. (The noise level σ_k in eq. [3] is arbitrarily set to unity.) The behavior of χ^2 with assumed inclination is rather weak, and for real data in the presence of noise cannot be used to accurately determine the true inclination of the star. It is advantageous that the resulting solutions are

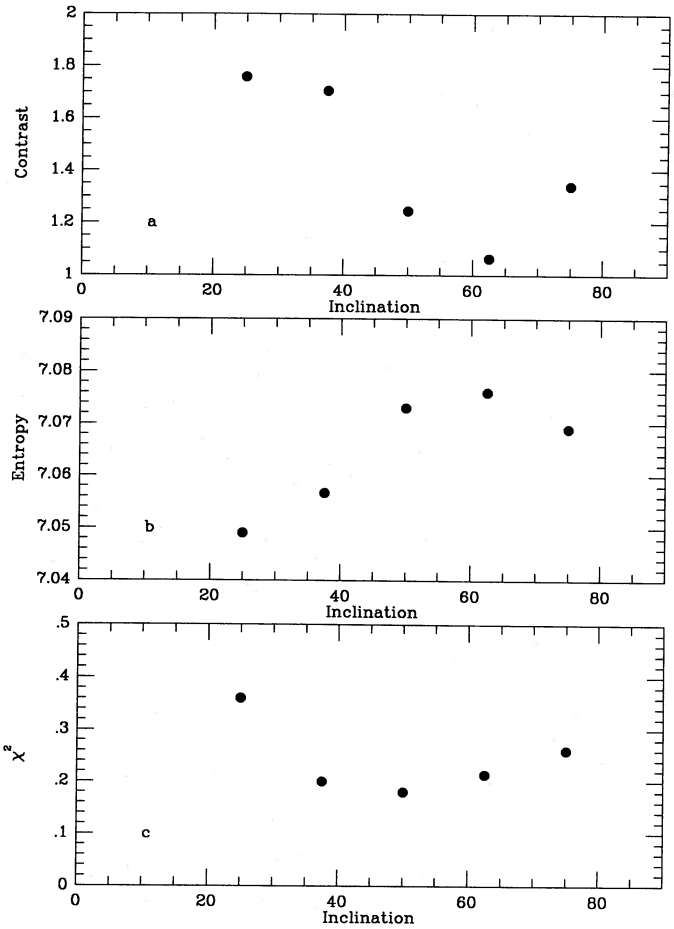

FIG. 7.—(*a*) The behavior of the contrast (defined as the ratio of the difference between maximum and minimum pixel values in the reconstructed image to the average pixel value) as a function of the inclination of the star assumed by the transfer matrix. The "true" inclination of the synthetic star used in generating the "observed" line profiles is 50°. (*b*) Behavior of the entropy as defined by eq. (2) of the reconstructed image as a function of the inclination used in the inversion process. (*c*) Behavior of χ^2 as defined by eq. (3) ($\sigma_k = 1$) as a function of assumed inclination.

insensitive to changes in the assumed inclination by $\pm 20°$. Reasonable estimates about the stellar radius can usually give us a value of the inclination to within these limits. However, the method may bring to our attention grossly wrong assumptions about the inclination (greater than 30° from the true inclination). This would manifest itself by the appearance of very strong features (very large or very small values of W_λ) concentrated at the lowest or highest latitudes as well as a difficulty of the method in fitting the observed profiles as manifested by higher values of χ^2.

e) Tests on Incorrect Assumptions of Line Shapes

Up to now the reconstructed equivalent width maps were constructed using scaled versions of the specific intensity profiles found in the transfer matrix. This presupposes that the intrinsic line shape is independent of the equivalent width. We now examine the effect of this assumption on the resulting image solution.

If the equivalent width of a spectral line in a spot becomes large, then its intrinsic shape can differ markedly from the intrinsic shape of the line profiles found in the transfer matrix.

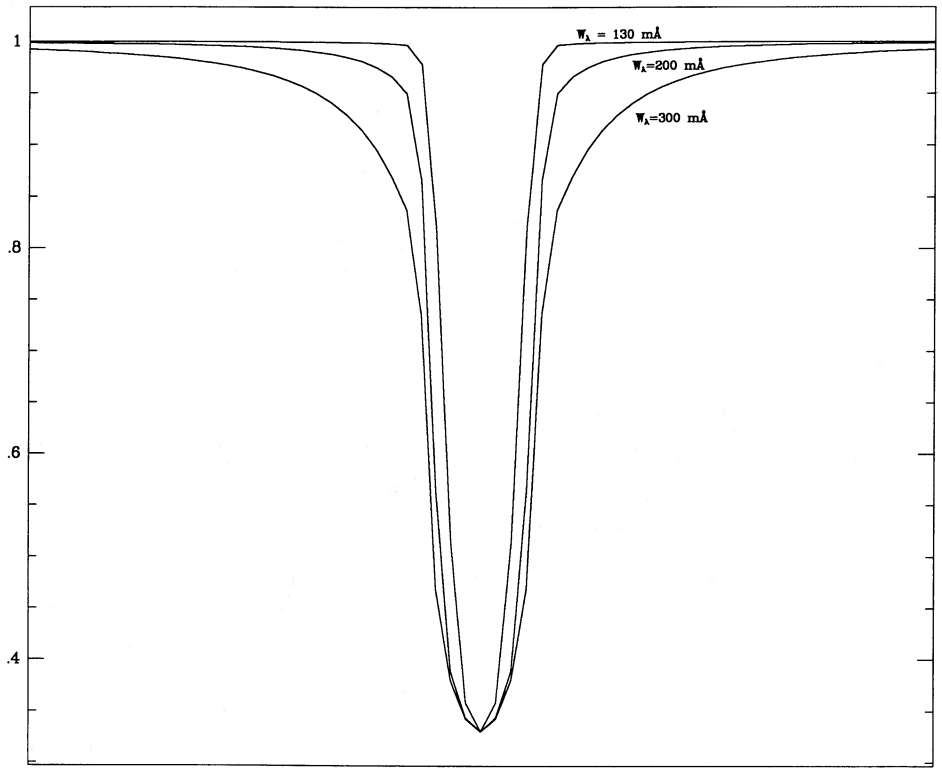

FIG. 8.—Illustration of the change in the shapes of the specific intensity line profiles as the equivalent width of the line is increased. The three line profiles were generated using Kurucz's atmospheres and ATLAS5 routines and have equivalent widths of 130, 200, and 300 mÅ. The line profiles were scaled so as to have the same depth.

Figure 8 illustrates the change in the spectral line shape as a function of increasing equivalent width. The figure shows three absorption lines generated from a Kurucz atmosphere and originally having equivalent widths of 130, 200, and 300 mÅ. The lines were rescaled so as to have the same depth. Here one sees the complications that may arise by using an incorrect line shape for constructing the transfer matrix used in the reconstruction process. For example, suppose that a spot on the star produced a spectral line with an equivalent width of 300 mÅ. If a transfer matrix was constructed with specific intensity profiles having the shape of the 200 mÅ profile in Figure 8, then it would lack the broad wings and have a smaller full width at half-maximum than the true line shapes in the spot. Intuitively, we would expect the reconstruction process to try to fit these wings by smearing features, primarily in longitude. The technique could then arrive at a slightly different solution depending on the equivalent width of the intrinsic profile used in generating the transfer matrix.

As a test of the sensitivity of the final image solution to changes in the line profiles shapes in $\boldsymbol{R}$, we performed four reconstructions using the spectral data of the "ring-spot-X" test case (input map of Fig. 4). In each case a different transfer matrix was constructed using specific intensity profiles of varying shapes (equivalent widths). The four profiles chosen had equivalent widths of 25, 130, 200, and 400 mÅ. The first two values represent the equivalent width found in the depleted spots and photosphere, respectively, while the 400 mÅ profile represents the shape of the intrinsic lines in the enhanced ring. The 200 mÅ was chosen as an intermediate value between photosphere and enhanced spot.

The maximum entropy reconstruction using the 25 mÅ line profiles is shown in the top two globes (phases 0.0 and 0.5) in Figure 9*a* and that for the 130 mÅ profiles in the lower two globes. The blurring of features for the 25 mÅ case is quite severe. The shape of the depleted "X" is barely discernible while the blurring of the overabundant ring is such that it seems to mask detection of the depleted spot as its center. The reconstruction using the 130 mÅ profile is significantly better. The shape of the "X" is easily distinguishable while the depleted spot at the center of the enhanced ring is becoming visible.

The reconstruction using the 200 mÅ line profiles is shown in the top two globes of Figure 9*b* and for 400 mÅ profiles in the lower two globes of the figure. The case using the 200 mÅ profile is also an adequate reconstruction and in some respects represents a marginally better solution than the previous case using the 130 mÅ profiles. The depleted spot at the center of the ring has become more pronounced and the ring itself is more uniform in shape. One drawback of this solution is that it blurs the lower regions of the "X". The reconstruction using the 400 mÅ profiles also recovers the gross features of the input map. However, this reconstruction marks the occurrence of the spurious "horns" from the top of the overabundant ring. These horns actually are a low-level band of overabundance which would completely encircle the star were it not interrupted by the presence of the depleted "X." Also note that the lower latitude regions of the "X" are severely blurred as well as the emergence of several low-level depleted spots near the equator. These depleted equatorial spots are an attempt by the method to remove the broad wings present in the profiles of the matrix elements but not present in the observed profiles. These equatorial spots would become more pronounced if we

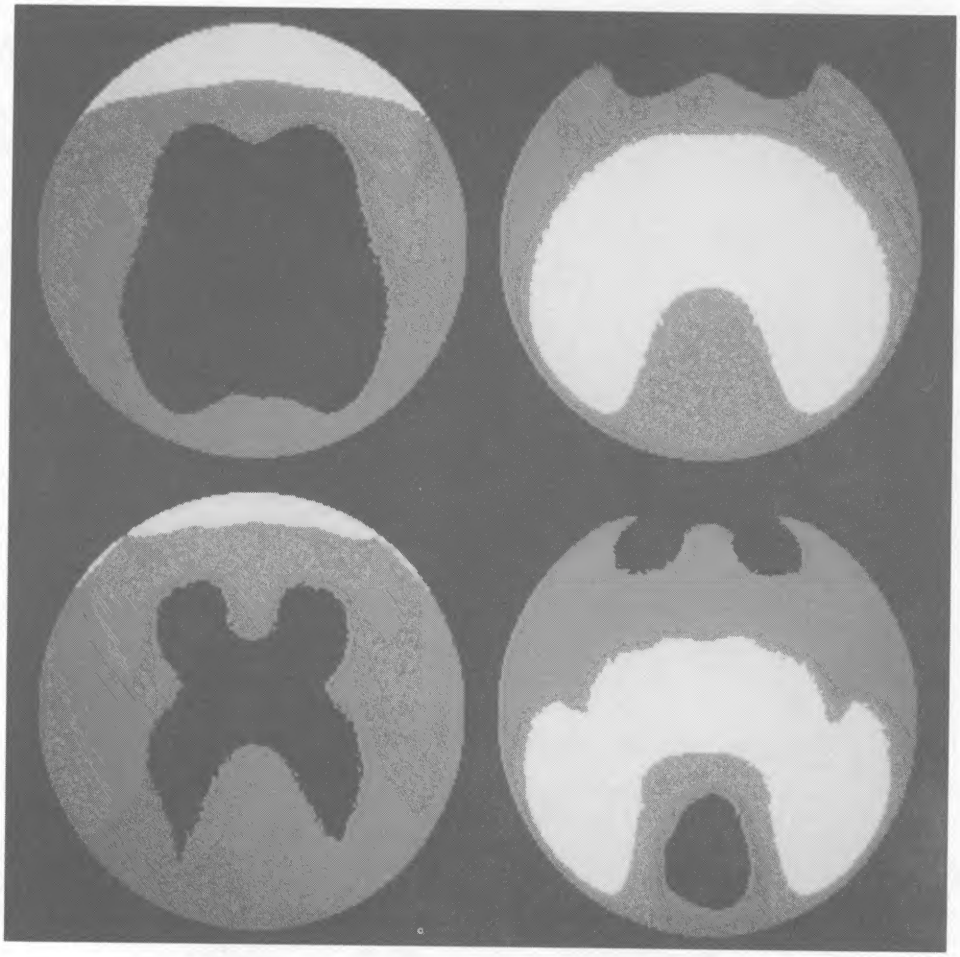

FIG. 9a

FIG. 9.—(*a*) Effects of incorrect assumptions of line shapes used on the transfer matrix. These are Doppler image reconstructions of the "ring-spot-X" test case using different specific intensity profiles (and thus different shapes) in the construction of the transfer matrix used in the inversion process. The top two globes (phase = 0.0 and 0.5) show the recovery using matrix elements which had a line shape consistent with flux profiles having an equivalent width of 25 mÅ. The bottom two globes are for a matrix constructed with 130 mÅ specific intensity profiles. (*b*) Same for (*a*) but for specific intensity profiles with $W_\lambda = 200$ mÅ (*top*) and $W_\lambda = 400$ mÅ (*bottom*) used in constructing the transfer matrix.

used an even stronger line profile in constructing our transfer matrix.

The best reconstructions are realized using the 130 mÅ (Fig. 9*a*, lower half) and 200 mÅ profile shapes (Fig. 9*b*, upper half) in the transfer matrices. These reconstructions also provide the best fit to the observed profiles. This is to be expected as both profiles represent a reasonable compromise between the shapes found in the photosphere and in the two types of spots. The poor reconstructions using the 25 mÅ and 400 mÅ profiles represent extreme examples and normally would not be encountered when modeling real data. These two values of equivalent widths are drastically different from the mean equivalent width of the observed profiles. In practice when constructing a transfer matrix, $\boldsymbol{R}$, one should chose specific intensity profiles whose equivalent widths are reasonably close to the mean value of the observed profiles. As long as this rule is adhered to, the resulting solutions are reasonably insensitive to the assumed shape of the specific intrinsic line profiles. Because of this insensitivity to assumed line shapes, we should expect that differences in the line shapes introduced by inclusion of the magnetic fields should have a small effect on the resulting equivalent width map.

V. NONLINEAR TREATMENT OF LINE SHAPES

Up to now the reconstruction technique has assumed that the local line shape was independent of its equivalent width, thus establishing a linear relationship between line depth and equivalent width. As demonstrated in § IV*e*, this assumption has little effect on the final image solution as long as the shapes of the specific intensity profiles used in constructing the transfer matrix were not grossly different from the true line shapes found on the surface of the star. However, an improvement in the method could be realized if the proper line shape for a given local equivalent width of a stellar pixel was used in the elements of the transfer matrix. Accomplishing this requires MEMSYS to have the ability to access the elements from a number of transfer matrices, each constructed using specific intensity profiles of different equivalent widths and thus slightly different shapes. As the pixel values of the image change, specific intensity profiles having the appropriate equivalent width would be shuffled into the matrix used by the MEMSYS package in transferring between image and data space. The amount of computer memory required for this scheme makes it cumbersome. A typical matrix $\boldsymbol{R}$ and its transpose require

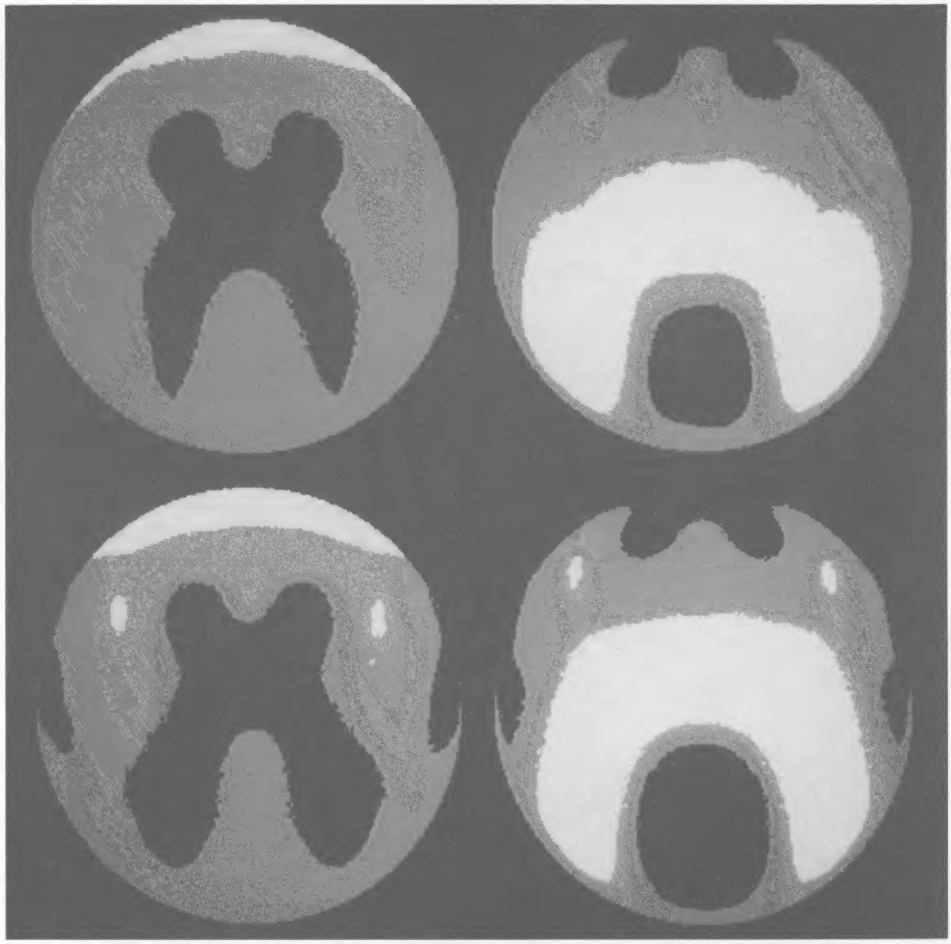

FIG. 9*b*

about 3 megabytes of memory and having access to a relatively small sample of five line shapes would require a large fraction of the total memory of our VAX. Although this could conceivably be done, it is very inefficient and execution of such a program requiring so much memory would slow the computer to an intolerable pace for all others.

However, not all elements of a given matrix are needed, only those elements required by those stellar pixels having the appropriate equivalent width. A more efficient scheme would be to carry around only those matrix elements actually required in the reconstruction process. Since we do not know *a priori* which matrix elements (and thus which specific intensity profiles) are required, these matrix elements must be calculated as needed. The iterative scheme for solving equation (1) makes it conducive to do this. Each iteration works independently from the previous iteration; the final image of an iteration is merely the initial guess for the next one. The algorithm should thus be insensitive to changes in the transfer matrix between iterations. Also as demonstrated in Paper I the final solution is insensitive to the initial guess for the image solution. Thus even though a different transfer matrix may initially result in a slightly worse fit to the observed data, the reconstruction process should quickly correct for these changes after one or two iterations. Ultimately an image is obtained which provides an adequate fit to the observed data as well as having the proper line shape as dictated by the local equivalent width.

Figure 10 shows a flow diagram for an algorithm which outlines this matrix element updating scheme as described below. Since the software to this algorithm is exterior to the MEMSYS package, it can easily be implemented without any modifications to MEMSYS itself. At the start of the reconstruction process a set of anywhere from 10–20 specific intensity line profiles as well as their equivalent widths are read. The line profiles associated with each equivalent width pixel are noted by the algorithm. It is imperative that the initial guess image be a uniform array whose value is the equivalent width of the specific intensity profile used in constructing the initial transfer matrix. (This is not the case when using constant line shapes throughout the reconstruction process.) At each iteration the algorithm checks to see if a recomputation of the matrix elements is required. Ideally the matrix elements should not be calculated after each iteration to allow the reconstruction process to recover from abrupt changes in the transfer matrix. Since most rapid changes in the image occur during the first iterations, the matrix is updated every second iteration. Toward the end of the reconstruction procedure (typically 20 iterations total) the pixels are changing less rapidly and a recalculation is not required as often. We found that after about the seventh iteration a recalculation every fourth iteration is sufficient and that after the fifteenth iteration there are no longer large changes in pixel values from iteration to iteration. At this point, matrix updating is stopped thus allowing MEMSYS to work with a fixed transfer matrix for the final five iterations.

If a recomputation of the matrix elements is required after

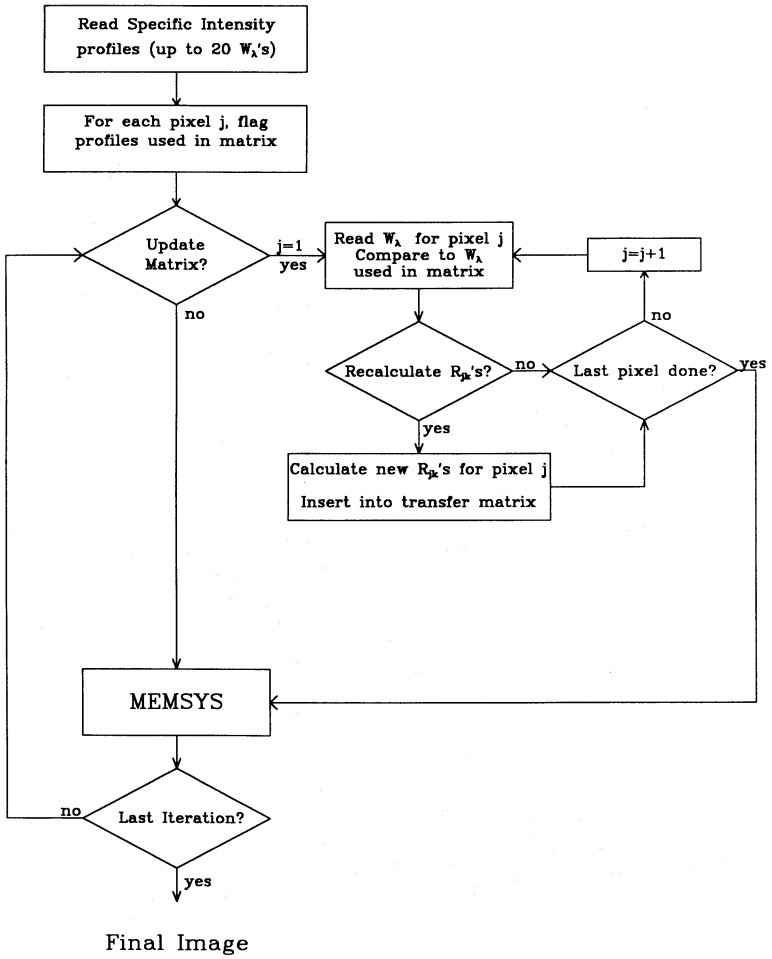

FIG. 10.—Flow diagram of the algorithm used in a reconstruction procedure which accounts for the nonlinear change in line shapes as a function of line strength

an iteration then the algorithm examines each image pixel (equivalent width value) and determines which specific intensity profiles are appropriate for this value. If the correct specific intensity profiles for this equivalent width are different than those used in the transfer matrix, then matrix elements are constructed using the new specific intensity profiles. Thus the algorithm is able to access a large number of transfer matrices while using computer memory for only one transfer matrix. This, in essence, is a "virtual" three-dimensional transfer matrix. The price paid for this savings in space is the increased computing time for those iterations where new matrix elements are recalculated. Depending on the complexity of the final image this matrix updating adds about 5–10 CPU minutes to a reconstruction process consisting of a total of 20 iterations, a relatively small amount of time compared to the 30–40 minutes required for a solution made with constant matrix elements.

The algorithm for the nonlinear treatment of the line shapes was tested on the ring-spot-X test case (Fig. 4) from § IV*b* with the results shown in Figure 11. The top two globes (phases 0.0 and 0.5) show the earlier reconstruction using a constant transfer matrix constructed with specific intensity profiles having an equivalent width of 200 mÅ. The lower two globes show the reconstruction using the updating matrix algorithm. In this figure the threshold level of the displayed pixels was lowered so as to bring out the subtle, spurious features due to the incorrect line profile shapes in the transfer matrix. This thresholding is the same for both reconstructions shown in Figure 11. An improvement in the final image solution is indeed realized. Spurious features such as the underabundant spots near the equator (black spots) have disappeared. Both the "X" and the ring are much sharper and are nearer to the true size of the input features, thus resulting in an improved reconstruction. It should be pointed out that even though using this modification to account for the changes in the line shape does make for a slightly better reconstruction, the procedure of using a constant line shape actually does extremely well. The gross features of the input map (Fig. 4) are recovered in both reconstructions, and in practice (when modeling real data) no significance anyway would be placed on the low-level spurious features which appear for the reconstruction using constant line shapes.

VI. APPLICATION TO γ^2 ARIETIS

a) Data Acquisition and Reduction

The method was used for mapping the silicon distribution on the surface of the Ap star γ^2 Ari (γ Ari S) using the λ6347 line of Si II. This line was chosen for its adequate strength and its relative freedom from blends. The data set was obtained using the 3 m telescope at Lick Observatory, with a TI 800 × 800 three-phase CCD (Robinson and Osborne 1986) detector mounted on the 203 cm (80″) camera of the coudé

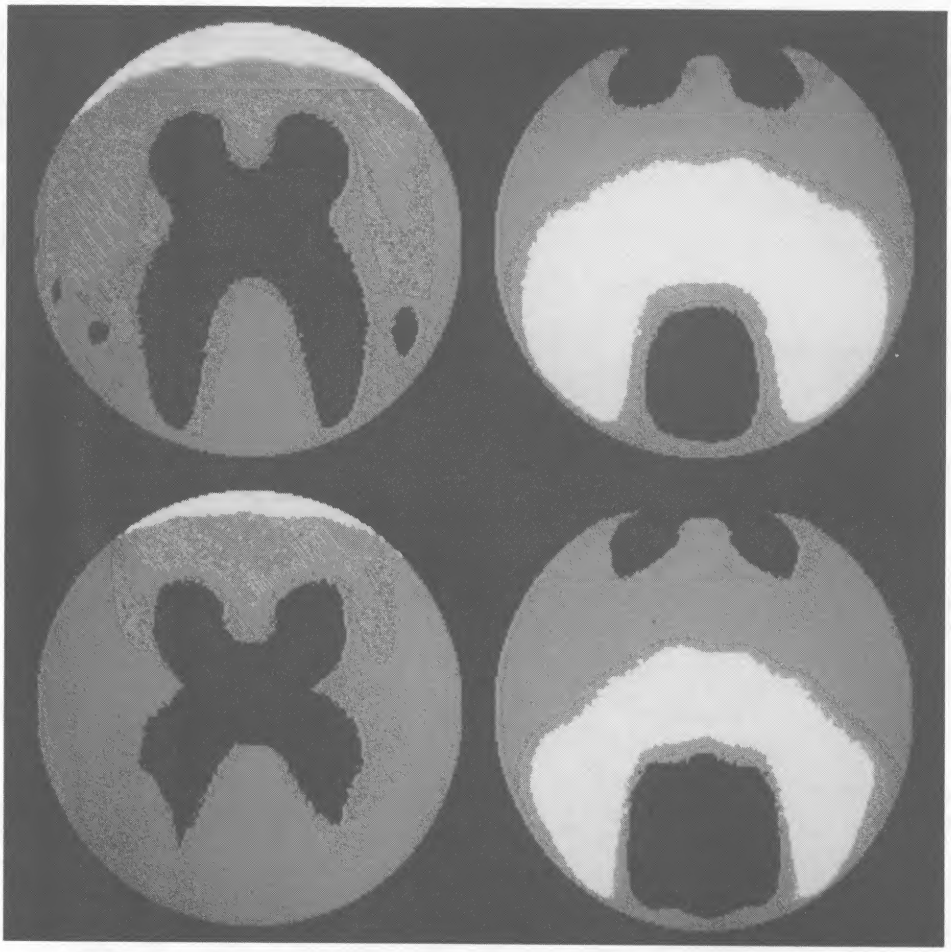

FIG. 11.—Doppler image recovery of the "ring-spot-X" test case of Fig. 4 using constant line shapes in the transfer matrix (*top*) and an updating matrix which changes the matrix elements as the local equivalent width of a pixel changes.

spectrograph. The spectral resolution for the observations was 3 pixels or 0.13 Å. A modified Bowen-Walraven image slicer was used to reformat the light from a 3″ diameter hole to a 0″67 slit. Use of the slicer accomplished two things. First, the slicer minimized slit losses due to seeing, and secondly, it "cooled" down the image in one dimension at the detector by spreading the light over a larger area of the CCD, thus allowing a higher total photon count to be obtained without saturation of any of the CCD pixels. The slicer, depending on seeing, typically spread the light over 100–150 columns of the CCD. An added advantage of this setup was that exceptional flat-fielding was achieved for the final reduced spectra. Although the pixel-to-pixel variations were removed by dividing each spectrum by an observation of a continuum source, we found that summing over 100–150 CCD image pixels to produce one spectral pixel was an excellent way of eliminating any additional systematic pixel-to-pixel variations. With this setup we have achieved signal-to-noise ratio values of up to 700 per pixel. Typical signal-to-noise ratio for the γ^2 Ari data set is 300–500 per pixel with each pixel being about one-third of a resolution element.

An immediate problem encountered during the data reduction is that the position of the λ6347 line of Si II coincides with two strong atmospheric water vapor lines. These water vapor lines are removed by subtracting the spectrum of a rapidly rotating early B star. Early B stars have no strong lines in this region of the spectrum, and any weak lines which may be present are severely Doppler-broadened. The resulting spectrum of the early star at λ6347 is thus largely that of atmospheric water. Figure 12 (*top*) shows a spectrum of the λ6347 region of ϵ Per, a B0.5 V star with a rotational velocity of 126 km s^{-1}. The absorption features visible are due to atmospheric water vapor. Each Si II observation is accompanied by one of an appropriate water standard. To remove the atmospheric features, the continua of the Ap star and water standard spectra are flattened using a spline function, normalized, and the continuum value subtracted. The atmospheric features of the water spectra are then scaled so that they match the depth of the respective lines in the Ap star spectrum. The water spectrum is then subtracted from the spectrum of interest. Figure 12 (*center*) shows the Si II λ6347 Å line of γ^2 with the telluric features present. Figure 12 (*bottom*) shows the same observation after using the ϵ Per spectrum to remove the water features. The dashed line shows the original spectrum with the water features present. The signal-to-noise ratio in the data is so high that the water features are removed to at least the level of the noise in the data. Observations taken for γ Ari at the same rotation phase but with the telluric features having different strengths produced identical looking profiles after removal of the telluric features. Also any residual water vapor features remaining in the line profiles are not phase-locked to a star's rotation period, and as a result, the reconstruction process tends to ignore these features in the line-fitting procedure. As a

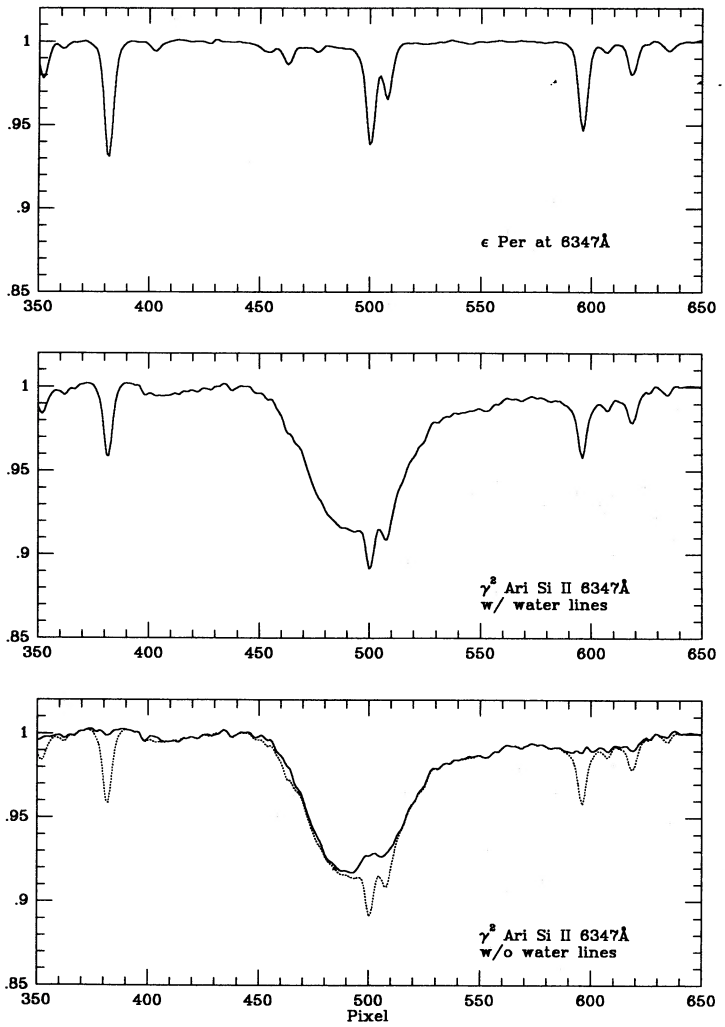

FIG. 12.—(*top*) Spectrum of ϵ Per near λ6347 showing the atmospheric water vapor lines. (*center*) Observation of γ^2 Ari in the same spectral region as ϵ Per. (*bottom*) γ^2 Ari observation with water features removed using spectrum of ϵ Per (*dashed line*).

test we created a data set stimulating a worst case scenario. Water lines of random strength and radial velocity were added to each phase of the data set for the "two-ring" test case. The resulting reconstruction showed no noticeable changes from the reconstruction shown in Figure 3 which was made without the addition of the water features. We are quite confident that any residual features resulting from improper removal of telluric features does not add any spurious features to the final image.

b) Silicon Distribution

γ Ari is a B9pSiCr star with variations in both silicon and chromium. Borra and Landstreet (1980) measured an effective magnetic field strength which varied between -1.0 and $+0.5$ kG and with a period of $1^d.6093 \pm 0^d.002$. Our spectral investigation yields a refined period of $1^d.60920 \pm 0^d.00004$. The measured $v \sin i$ for this star was 60 km s^{-1}. An inclination of 55° was used in the modeling, which results from assuming a main-sequence radius of 2.5 $R_\odot$ for γ^2 Ari. Models were run at several inclinations ranging from 70° to 40° and resulted in no significant changes in the derived abundance distribution. Figure 13 represents the maximum entropy equivalent width map and Figure 14 the fit to the observed line profiles produced from this map (crosses again represent observed data and lines represent the maximum entropy fit). The silicon image is shown at intervals of 0.125 in phase starting with phase 0.0 for the upper left-hand globe and the rotation sequence proceeding left to right and top to bottom. The ephemeris used for this phasing was 2,446,279.972 + 1.60920*E*. Once again, white represents overabundance with respect to the mean value of the star, and black represents underabundance. The most obvious feature is a prominent underabundant spot of radius 15° situated at 35° latitude and at phase 0.67. The mean value of the equivalent width in this spot is 30 mÅ. The mean equivalent width over the total surface of the star is about 170 mÅ. This spot is very near the longitudinal position of the negative magnetic pole as measured by Borra and Landstreet (1980). Surrounding this spot is an incomplete annulus of overabundance extending in radius from about 30° to 60° and reasonably well centered on the underabundant spot. Although not readily visible in this high-contrast view of the image, the ring is nonuniform in strength having its maximum value of 550 mÅ in a patch below the underabundant spot. The smallest value of the equivalent width in this ring is about 250 mÅ while the average over the annulus is about 300 mÅ. A weak second underabundant spot also appears at 0° latitude and situated 160° in longitude from the first. The local equivalent width in this spot is about 60 mÅ.

VII. DISCUSSION

One promising explanation for the abundance variations on the surface of the Ap stars is the selective diffusion mechanism first proposed by Michaud (1970) and elaborated on by many researchers since then. In a stable stellar atmosphere the radiation force transferred to elements by bound-bound or bound-free transitions works against gravity. If an element has suitably placed lines in spectral regions where there is large stellar flux, then the radiation force can overcome the gravitational force, and the element will migrate upward, creating apparent overabundances. Elements for which gravity is the dominant force acting upon them should diffuse downwards, creating apparent underabundances. The presence of magnetic fields modifies the diffusion mechanism by suppressing the motion of ions across the field lines. In regions of the stellar atmosphere where the collisional frequency is low, ions will primarily move along field lines so that vertical diffusion can occur only where the field lines are vertical.

Work on the diffusion of silicon in the presence of magnetic fields by Vauclair, Hardorp, and Peterson (1979) and Alecian and Vauclair (1981) suggests that this element, which sinks as an ion but rises as a neutral, should accumulate where the field lines are horizontal. If this is the case, then for a pure dipole field one expects an overabundant band of silicon surrounding the magnetic equator. The location of this band is modified by the presence of a quadrupole component or by decentering the dipole. In both cases the position of the band is shifted to higher magnetic latitudes (Michaud, Méggesier, and Charland 1981). Since silicon spends most of its time in the singly ionized state in the atmospheres of Ap stars, then we would expect a downward migration of silicon at places where the diffusion is unobstructed by the field lines, namely the poles.

The silicon image of γ^2 Ari thus seems consistent with this diffusion scenario. We propose that the underabundant spot at phase 0.67 actually represents the location of the negative mag-

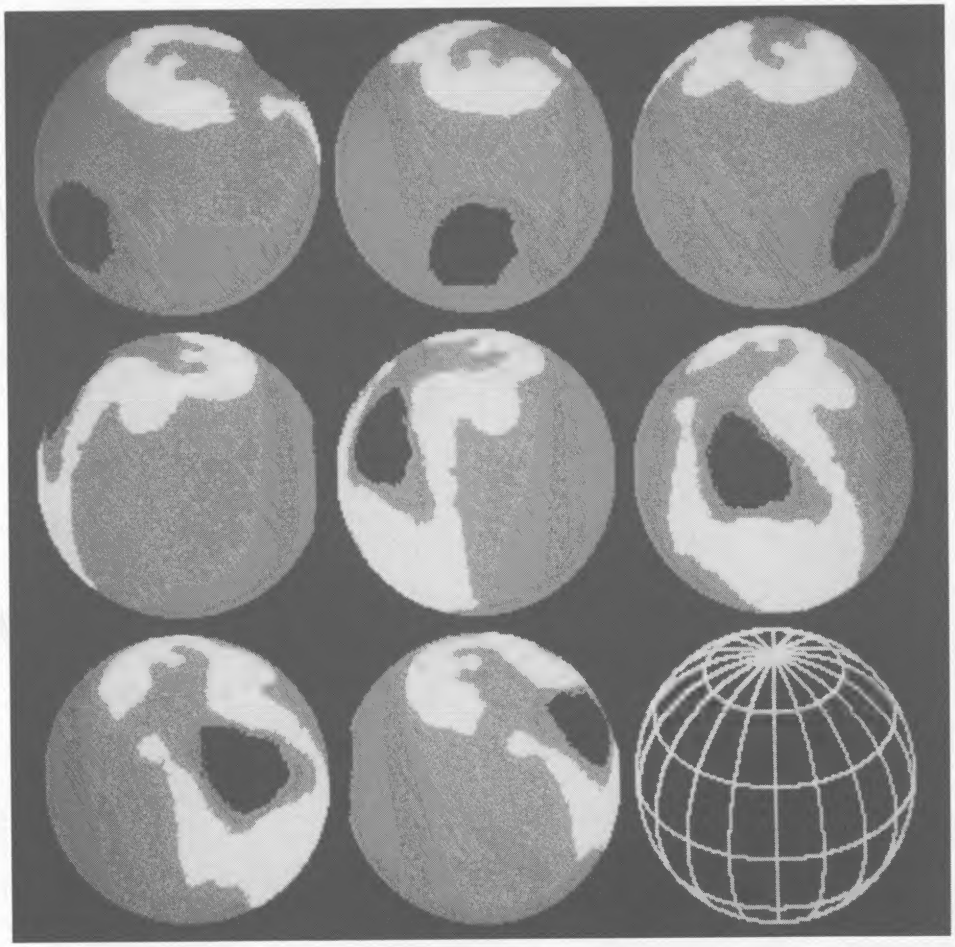

FIG. 13.—Doppler image reconstruction of the local equivalent width of the Si II λ6347 Å line in γ^2 Ari, shown at eight equidistant phases. An inclination of 55° was assumed in the reconstruction. White shows regions of enhanced abundance (large local equivalent width) black represents depleted abundance (small local equivalent width). Once again the star is shown at intervals of 0.125 in phase starting with phase 0.0 in the upper left-hand corner.

netic pole of the star and that the weaker spot near phase 0.13 is the positive pole. If this is true, then the obliquity angle for the magnetic field is approximately 55° based on the location of the strong depleted spot at high latitudes. As demonstrated by our test cases, the method has a more difficult time reconstructing features at the lowest latitude. Thus the latitudinal position of the weak depleted spot at phase 0.13 is more poorly defined. It actually may be stronger (lower equivalent width) and at a lower latitude. Unlike modeling of the magnetic field measurements, this obliquity angle is well determined, as there is a characteristic feature to mark the magnetic pole. The location of this feature with respect to the rotation axis is well determined in spite of uncertainties in the stellar inclination.

Whether depleted spots of silicon appear at the poles of all Ap stars will be established with additional Doppler images of other stars. If true, then these spots provide an accurate measurement of the obliquity angle for the field in spite of uncertainties in the inclination of the star. As pointed out previously, the method is insensitive to wrong values of the assumed inclination. Features will be placed at the same position in the fixed frame of the star regardless of our assumptions about the inclination of the star.

There are two features to note about the enhanced abundance annulus. First, it appears to be very near the negative magnetic pole and it is strongest on the side preceding the passage of the depleted spot. This is obvious from the observed spectral line profiles since a large increase in the equivalent width of the line is observed at phases 0.43 to 0.64, but the opposite side of the star seems to be devoid of such a feature. If diffusion theory holds and this represents regions where the field lines are horizontal, then this annulus appears at a much higher magnetic latitude than can be accounted for by a pure dipole field. This suggests that either the dipole is decentered in the direction of the negative pole or that a strong quadrupole component to the overall dipole field is present.

The broken and nonuniform strength of the annulus is a very real feature and not merely an artifact of incomplete phase coverage. The largest time gap in the data is only 0.14 of a rotation phase, and simulations have shown that the method should be able to recover a complete annulus with the same phase coverage of the data set. One possible way of producing an incomplete or nonuniform annulus is to allow for a decentered, nonaxisymmetric dipole. This would cause the horizontal field strength at the surface to be stronger on one side of the annulus. Stift (1975) has shown that such a dipole can indeed reproduce the magnetic field variations in many Ap stars. Alternatively, small amounts of macroturbulence or meridional currents may serve to break up the continuity of

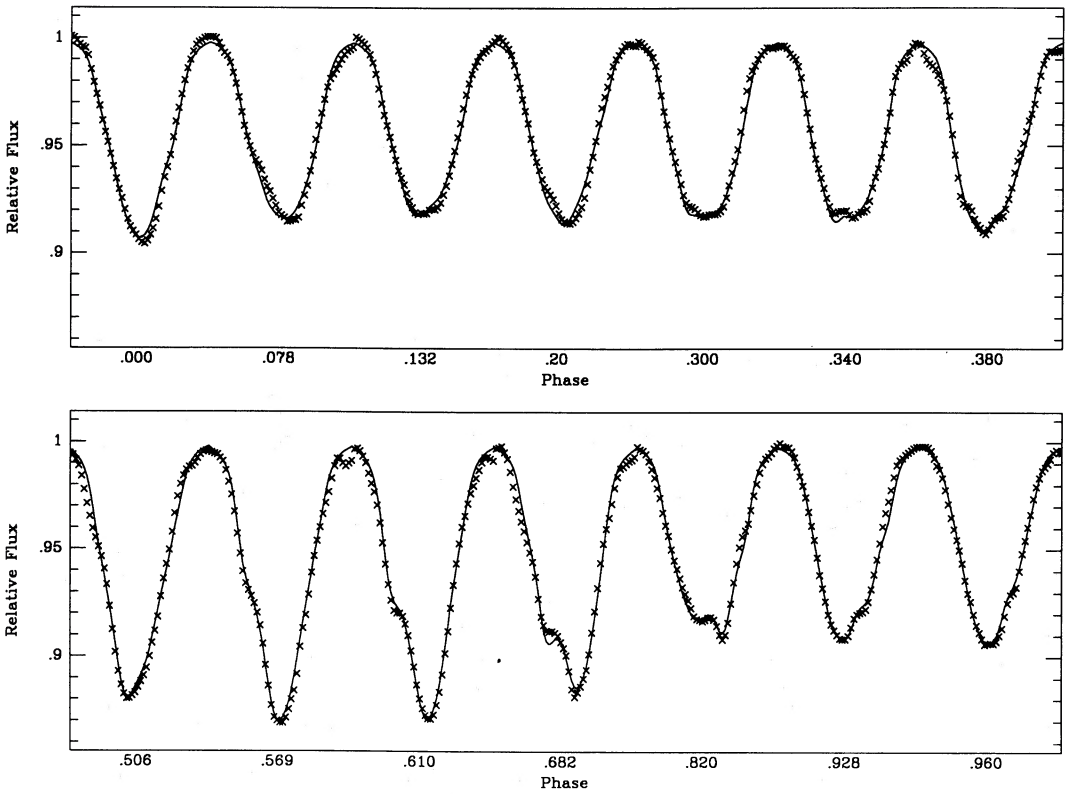

FIG. 14.—The flux profiles for the Si II line of γ^2 Ari for the various observed phases. Crosses represent the observed data, while a line is drawn for the flux profiles produced by the map in Fig. 13.

the ring. A clearer picture of the true behavior of silicon in these stars should emerge with the acquisition of additional Doppler images of other stars.

VIII. SUMMARY

We have shown that the improved form of the Doppler imaging technique can be used to obtain accurate maps of the surface distribution of elements on rapidly rotating Ap stars strictly from the spectral line variations. Not only can the method accurately recover complex spot distributions such as rings but it also is able to reconstruct spot distributions with both depleted *and* enhanced abundance regions in spite of the assumption that the intrinsic line profile for both regions is the same. The technique is rather insensitive to reasonable assumptions about the intrinsic shape of the specific intensity profiles and the inclination of the star. The technique was applied to the B9pSiCr star γ^2 Ari using the Si II λ6347 Å line. The resulting reconstruction shows that silicon is depleted near the magnetic poles and that it is enhanced in an incomplete, nonuniform annulus near the negative magnetic pole. This image appears to be consistent with the predictions of diffusion theory if γ^2 Ari has a quadrupole component or is a decentered dipole, and provides direct observational support for the theory that diffusion is indeed the process responsible for the abundance variations in the Ap stars. In forthcoming papers applications of this technique to a selection of silicon and chromium variables will be presented.

We would like to thank Dr. Keith Horne for bringing the MEMSYS software package to our attention, and to Dr. Steve Gull for kindly making it available to us. Also this project could not have been successfully undertaken were it not for the large amounts of observing time on the Shane 3 m telescope made available to us by Dr. Robert Kraft and the time allocation committee. This work was supported by NSF grant AST-8210202, whose support we gratefully acknowledge.

REFERENCES

Alecian, G., and Vauclair, S. 1981, *Astr. Ap.*, **101**, 16.
Borra, E. F., and Landstreet, J. D. 1980, *Ap. J. Suppl.*, **42**, 421.
Deutsch, A. J. 1970, *Ap. J.*, **159**, 985.
Falk, A. E., and Wehlau, W. H. 1974, *Ap. J.*, **192**, 409.
Goncharsky, A. V., Ryabchikova, T. A., Stepanov, V. V., Khokhlova, V. L., and Yagola, A. G. 1983, *Astr. Zh.*, **60**, 83 (English trans. in *Soviet Astr.*, **27**, 49).
Goncharsky, A. V., Stepanov, V. V., Khokhlova, V. L., and Yagola, A. G. 1982, *Astr. Zh.*, **59**, 1146 (English trans. in *Soviet Astr.*, **26**, 690).
Khokhlova, V. L., Rice, J. B., and Wehlau, W. H. 1986, *Ap. J.*, **307**, 768.
Kurucz, R. L. 1979, *Ap. J. Suppl.*, **40**, 1.
Mégessier, C. 1975, *Astr. Ap.*, **39**, 263.
Michaud, G. 1970, *Ap. J.*, **160**, 640.
Michaud, G., Méggesier, C., and Charland, Y. 1981, *Astr. Ap.*, **103**, 244.
Mihalas, D. 1973, *Ap. J.*, **184**, 851.
Pavlova, V. M., Khokhlova, V. L., and Aslanov, I. A. 1977, *Astr. Zh.*, **54**, 979 (English trans. in *Soviet Astr.*, **21**, 554).
Pyper, D. M. 1969, *Ap. J. Suppl.*, **18**, 347.
Rice, J. B., Wehlau, W. H., Khokhlova, V. L., and Piskunov, N. E. 1981, in *Upper Main Sequence Chemically Peculiar Stars*, ed. J. Renson (Liège: University of Liège), p. 265.
Robinson, L., and Osborne, J. 1986, *Proc. SPIE, Instrumentation in Astronomy VI*, **627**, 492.

Skilling, J., and Bryan, R. J. 1984, *M.N.R.A.S.*, **211**, 111.
Skilling, J., and Gull, S. F. 1981, Algorithms and Applications, presented at Workshop on Maximum Entropy, Laramie, Wyoming.
Stibbs, D. W. N. 1950, *M.N.R.A.S.*, **110**, 395.
Stift, M. J. 1975, *M.N.R.A.S.*, **172**, 133.
Vauclair, S., Hardorp, J., and Peterson, D. M. 1979, *Ap. J.*, **227**, 526.
Vogt, S. S., Penrod, G. D., and Hatzes, A. P. 1987, *Ap. J.*, **321**, 496 (Paper I).

ARTIE P. HATZES, G. DONALD PENROD, and STEVEN S. VOGT: Lick Observatory, Board of Studies in Astronomy and Astrophysics, University of California, Santa Cruz, CA 95064